Supplement of Earth Syst. Dynam., 16, 1103–1134, 2025
https://doi.org/10.5194/esd-16-1103-2025-supplement

Earth System Dynamics
Open Access

Supplement of

Earth's future climate and its variability simulated at 9 km global resolution

Ja-Yeon Moon et al.

Correspondence to: Thomas Jung (thomas.jung@awi.de) and Axel Timmermann (axel@ibsclimate.org)

Contents of this file

- Method for Okubo-Weiss-Zeta Parameter with equations (S1-S2)
- Table S1 to S2
- Figures S1 to S17

Equations (S1-S2):

The OWZP is a resolution independent tracking method to detect tropical cyclones (Tory et al., 2013b, a). It primarily relies on Okubo-Weiss Parameter and other large-scale variables that are interpolated to 1°×1° grid. Here we provide a brief introduction to the OWZP tracking scheme. The detailed algorithm is explained in the references.

The Okubo-Weiss Parameter is a measure of the low-deformation vorticity

$$OW = \xi^2 - (E^2 + F^2) \quad \text{(S1)}$$

where $E = \left(\frac{\partial u}{\partial x}\right) - \left(\frac{\partial v}{\partial y}\right)$ and $F = \left(\frac{\partial v}{\partial x}\right) + \left(\frac{\partial u}{\partial y}\right)$ are the square of the stretching and shearing deformation, respectively. Then, Okubo-Weiss-Zeta parameter is calculated by calculating vertical component of absolute vorticity ($\eta = \xi + f$) weighted by $OW_{norm} = [\xi^2 - (E^2 + F^2)]/\xi^2$ and multiplied by the sign of Coriolis parameter f for a consistent cyclonic vorticity in both hemispheres:

$$OWZ = \eta \times (OW_{norm}, 0) \ \times sign(f) \quad \text{(S2)}$$

Therefore, OWZ and absolute vorticity have a similar magnitude, and the OWZ to η ratio gets smaller when the flow has strong deformation.

The potential to support TC formations is identified by the "initial" thresholds (Table SX) for OWZ at 850 hPa and 500 hPa, relative humidity at 950 hPa and 700 hPa, vertical wind shear between 850 hPa and 200 hPa, and specific humidity at 950 hPa. The threshold values were obtained from Raavi et al. (2023).

Neighboring grid points that meet the initial thresholds are merged together and create a single "clump", representing a storm at a specific time. Weaker and smaller in close proximity are eliminated. The identified clumps are then tracked forward in time until no clumps remain. At each position along the storm track, the storm is assigned individual values for OWZ, relative humidity, vertical wind shear, and specific humidity. If the updated values pass the "core" threshold (Table S1), it is labeled as "true". If a sequence of clumps meets consecutive "true" labels for 48 h or more, the storm is considered as a tropical cyclone. In our study, we utilized 6 hourly data, therefore, the criteria for identifying a tropical cyclone is based on the presence of nine consecutive "true" clumps along the track, with the ninth "true" position being designated as the location of storm genesis.

Table S1: Initial and core thresholds for tracking tropical cyclones (TCs) using Okubo–Weiss–Zeta parameter (OWZP) detection scheme.

Criterion	OWZ_{850}	OWZ_{500}	RH_{950}	RH_{700}	$VWS_{850\text{-}200}$	SH_{950}
Initial	$> 50\times10^{-6}\ s^{-1}$	$> 40\times10^{-6}\ s^{-1}$	> 70 %	> 50%	$< 25\ m\ s^{-1}$	$>10\ g\ kg^{-1}$
Core	$> 60\times10^{-6}\ s^{-1}$	$> 50\times10^{-6}\ s^{-1}$	> 85 %	> 70%	$< 12.5\ m\ s^{-1}$	$>14\ g\ kg^{-1}$

Table S2: Performance indices (Reichler and Kim, 2008) that give the absolute error in climatology of the last 11 years in (a) MR and (b) HR AWI-CM3 historical simulations as a fraction of the absolute error averaged over CMIP6 models. Values below (above) 1 correspond to below (above) CMIP6 average biases. The underlying observations against which all models were evaluated are OSI SAF OSI-450 (Lavergne et al., 2019) – sea ice concentration (siconc); MODIS Atmosphere L2 Cloud Product (Platnick et al., 2015) – cloud cover (clt); Global Precipitation Climatology Project (GPCP) Monthly analysis (Adler et al., 2018) – precipitation (pr); Clouds and the Earth's Radiant Energy System (CERES) (Wielicki et al., 1996) – TOA outgoing longwave radiation (rlut); ECMWF reanalysis ERA5 (Hersbach et al., 2023) – near- surface air temperature (tas), eastward near-surface wind (uas), northward near-surface wind (vas), 300 hPa eastward wind (ua), and 500 hPa geopotential height; NOAA Jason-1, Jason-2, and CryoSat-2 combined – sea surface height (zos); HadISST2 (Titchner and Rayner, 2014) – sea surface temperature (tos); EN4 (1900-1997) (Good et al., 2013) – ocean temperature (thetao) and salinity (so) at 10m, 100m, and 1000m. The list of CMIP6 models for climate model performance index calculation is ACCESS-CM2, AWI-CM-1-1-MR, BCC-CSM2-MR, CAMS-CSM1-0, CAS-ESM2-0, CanESM5, CIESM, CESM2, CMCC-CM2-SR5, CNRM-CM6-1-HR, FGOALS- f3-L, FIO-ESM-2-0, E3SM-1-1, EC-Earth3, GFDL-CM4, GISS-E2-1-G, HadGEM3-GC31-MM, ICON-ESM-LR, IITM-ESM, INM-CM5-0, IPSL-CM6A-LR, KIOST- ESM, NESM3, NorESM2-MM, MCM-UA-1-0, MIROC6, MPI-ESM1-2-LR, MRI-ESM2-0, SAM0-UNICON, and TaiESM1.

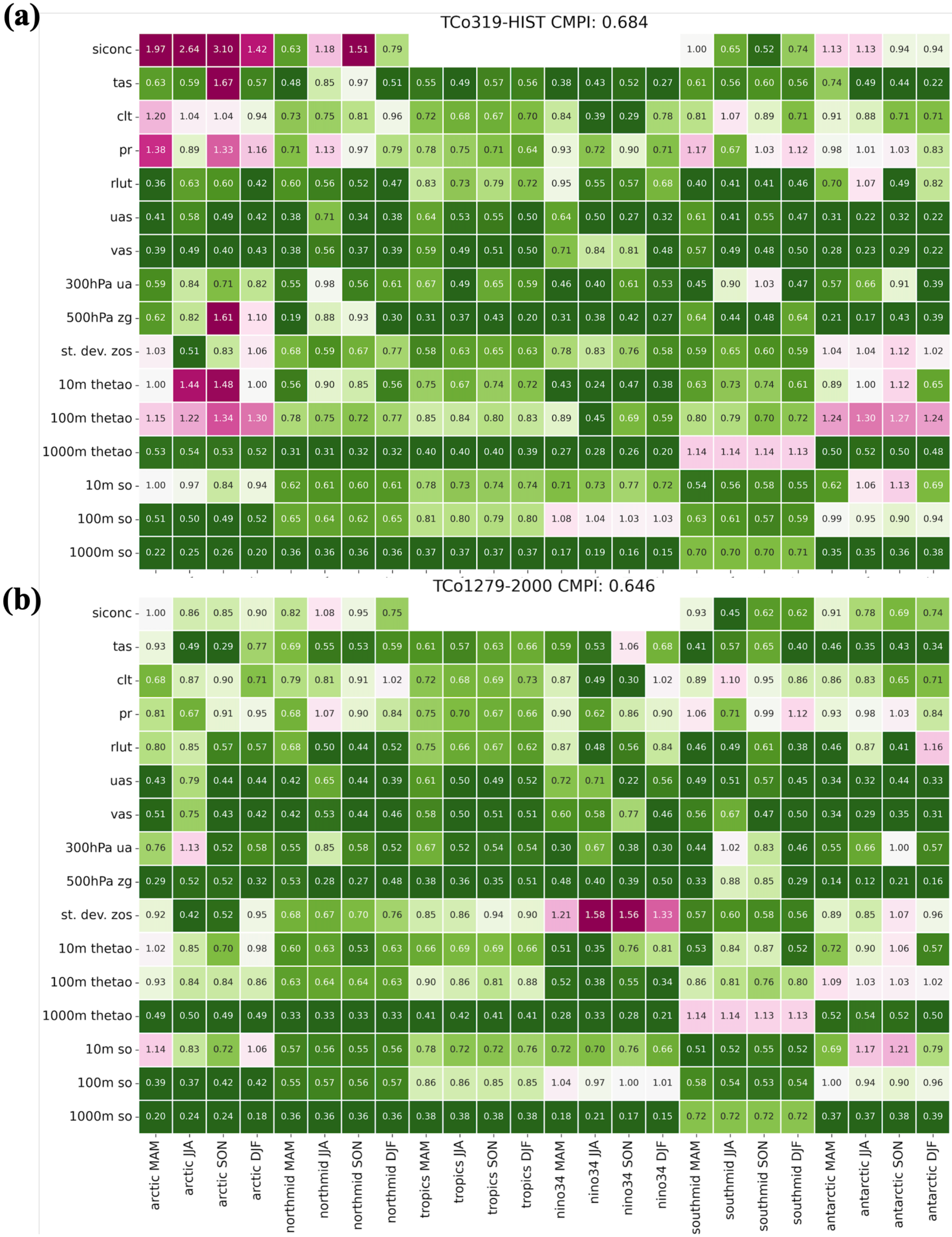
(a)
TCo319-HIST CMPI: 0.684
(b)
TCo1279-2000 CMPI: 0.646
siconc
tas
clt
pr
rlut
uas
vas
300hPa ua
500hPa zg
st. dev. zos
10m thetao
100m thetao
1000m thetao
10m so
100m so
1000m so
arctic MAM
arctic JJA
arctic SON
arctic DJF
northmid MAM
northmid JJA
northmid SON
northmid DJF
tropics MAM
tropics JJA
tropics SON
tropics DJF
nino34 MAM
nino34 JJA
nino34 SON
nino34 DJF
southmid MAM
southmid JJA
southmid SON
southmid DJF
antarctic MAM
antarctic JJA
antarctic SON
antarctic DJF

Figures S1 to S17:

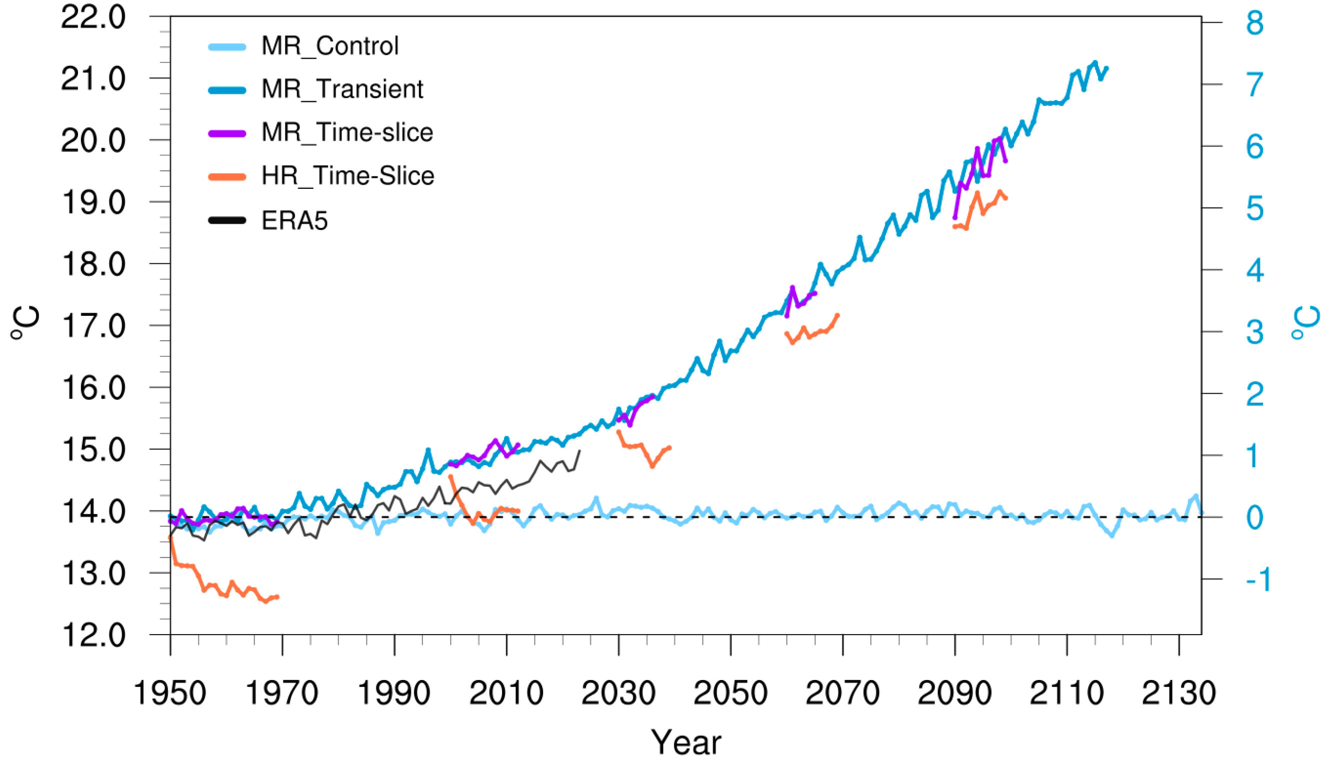

Figure S1: The simulated global mean temperatures in the MR simulation control run (light blue), MR historical and SSP5-8.5 simulation (dark blue), MR (purple) and HR (coral) 1950 control – historical - SSP5-8.5 time-slice simulations as well as an observational estimate from the ERA5 reanalysis (black).

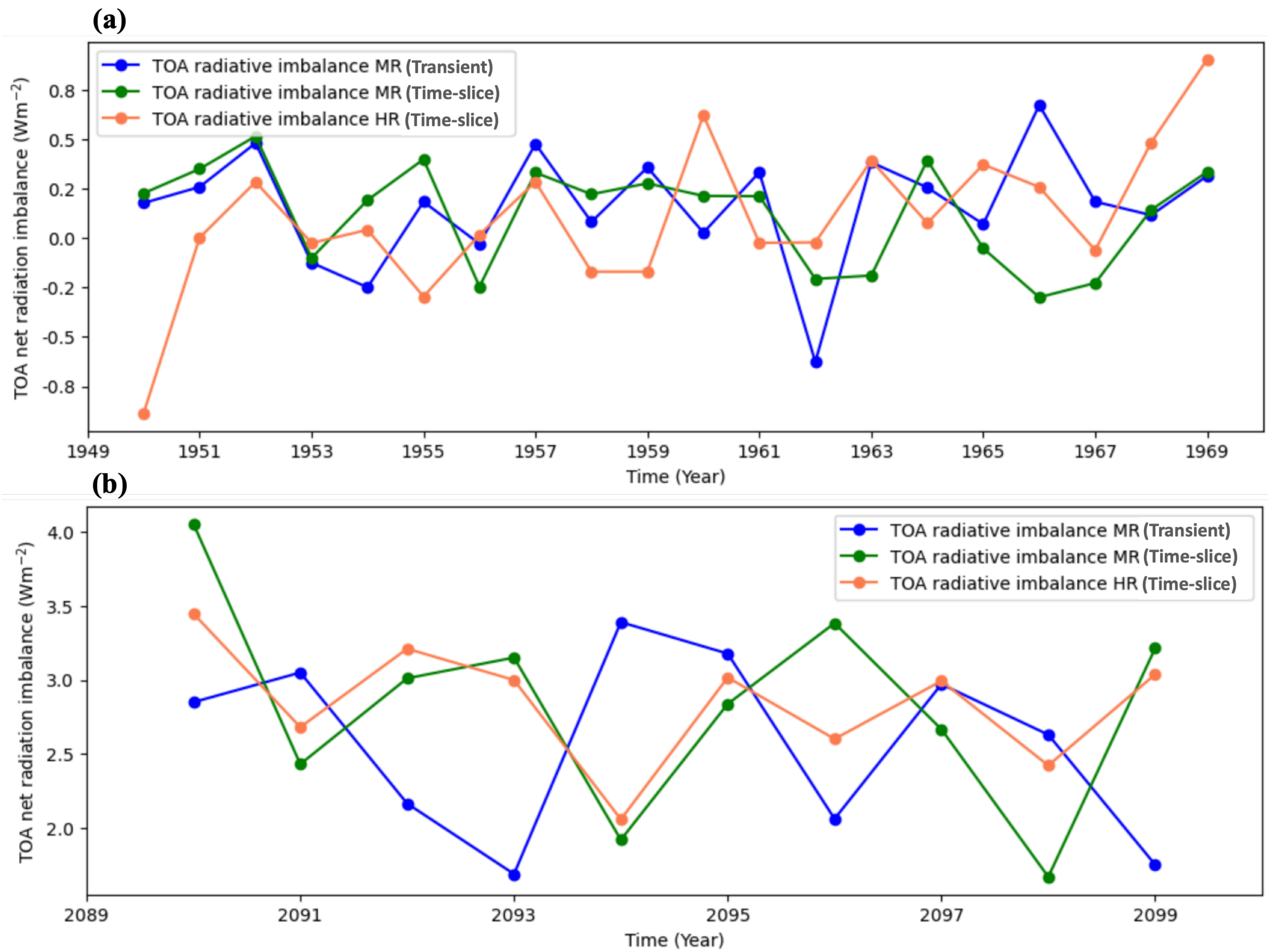

Figure S2: Global mean top of atmosphere (TOA) radiative imbalance calculated for (a) 1950~1969 MR transient control, MR time-slice, HR time-slice simulations and (b) 2090~2099 MR transient, MR time-slice, HR time-slice simulations.

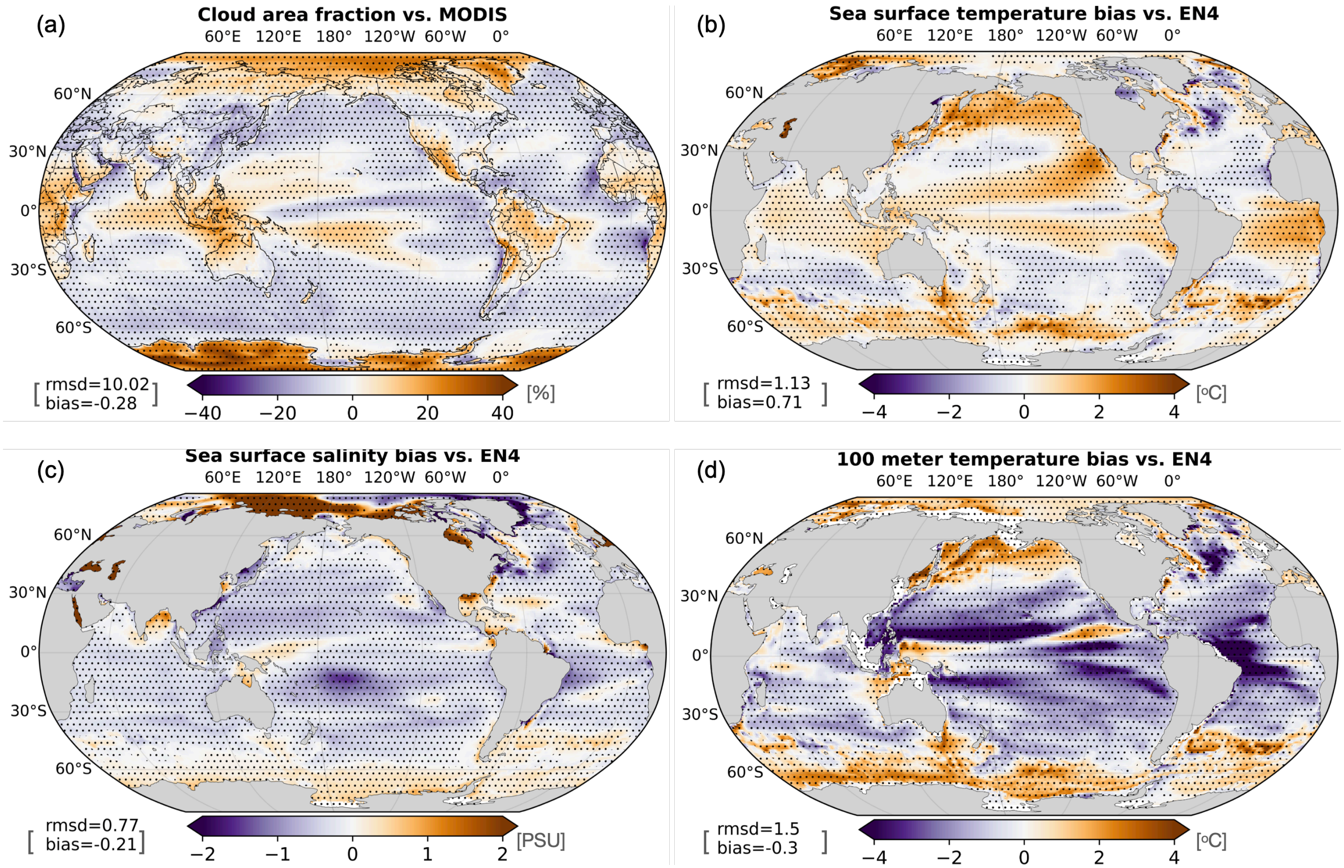

Figure S3: Bias map for MR historical simulation (2002-2012) for (a) total cloudiness (upper left) relative to MODIS cloud product (2000-2011) (Kato et al., 2018). Other panels: bias maps for (b) sea surface temperature, (c) sea surface salinity and (d) 100 m temperature relative to the observational EN4 climatology (1900-1997) (Good et al., 2013). Rmsd and bias refer to the root mean squared deviation and the global mean difference between model and reference product. The stippled areas where the null hypothesis can be rejected at the 95% confidence level by Welch's *t*-test. We used the default settings in the stats module SciPy (version 1.11.1) in Python, which applies Welch's t-test at every grid point allowing for unequal variances.

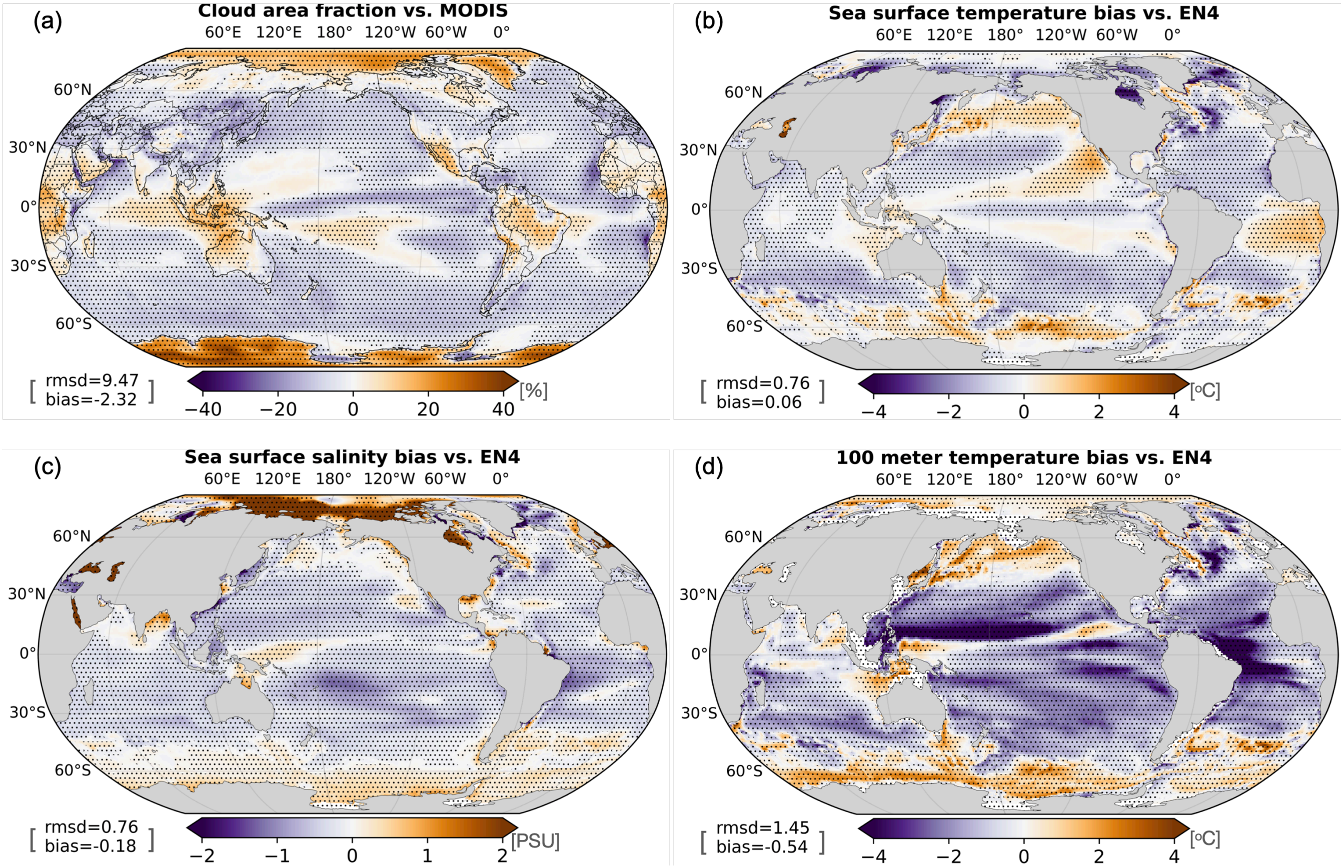

Figure S4: Bias map for HR historical simulation (2002-2012) for (a) total cloudiness (upper left) relative to MODIS cloud product (2000-2011) (Kato et al., 2018). Other panels: bias maps for (b) sea surface temperature, (c) sea surface salinity and (d) 100 m temperature relative to the observational EN4 climatology (1900-1997) (Good et al., 2013). Rmsd and bias refer to the root mean squared deviation and the global mean difference between model and reference product. The stippled areas where the null hypothesis can be rejected at the 95% confidence level by Welch's *t*-test. We used the default settings in the stats module SciPy (version 1.11.1) in Python, which applies Welch's t-test at every grid point allowing for unequal variances.

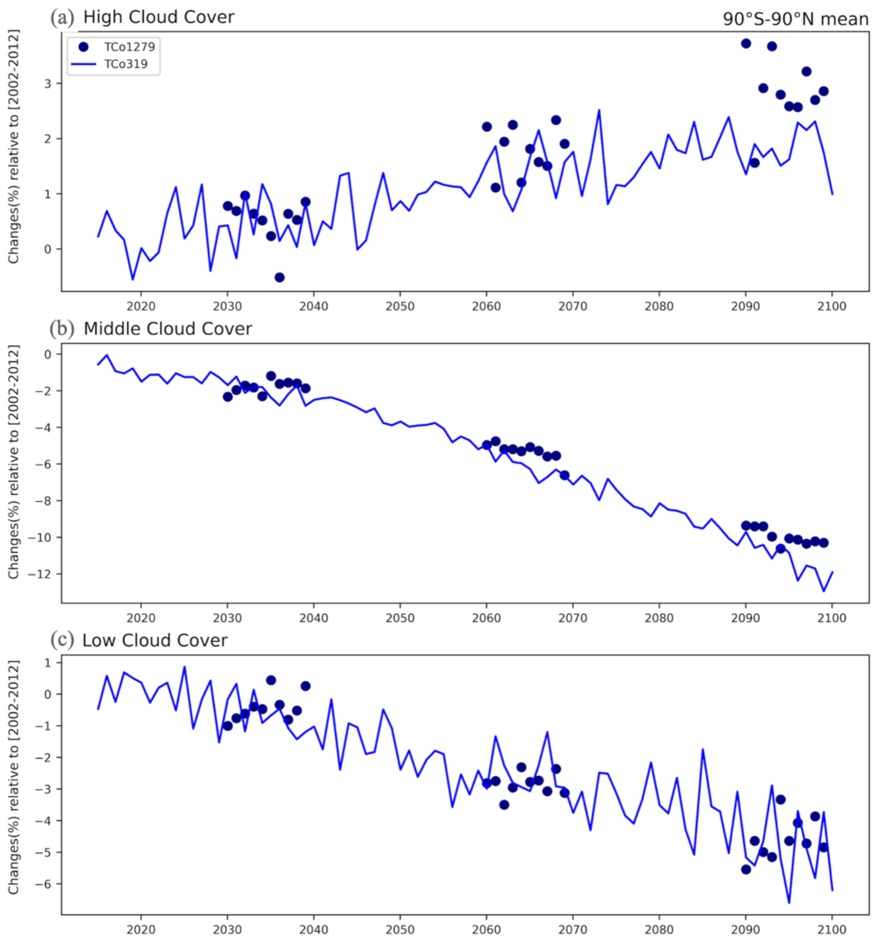

Figure S5: Annual mean difference of global mean (a) high, (b) middle, (c) low cloud cover in MR simulation (blue line) and HR (navy dot) snapshot simulations relative to 2000s.

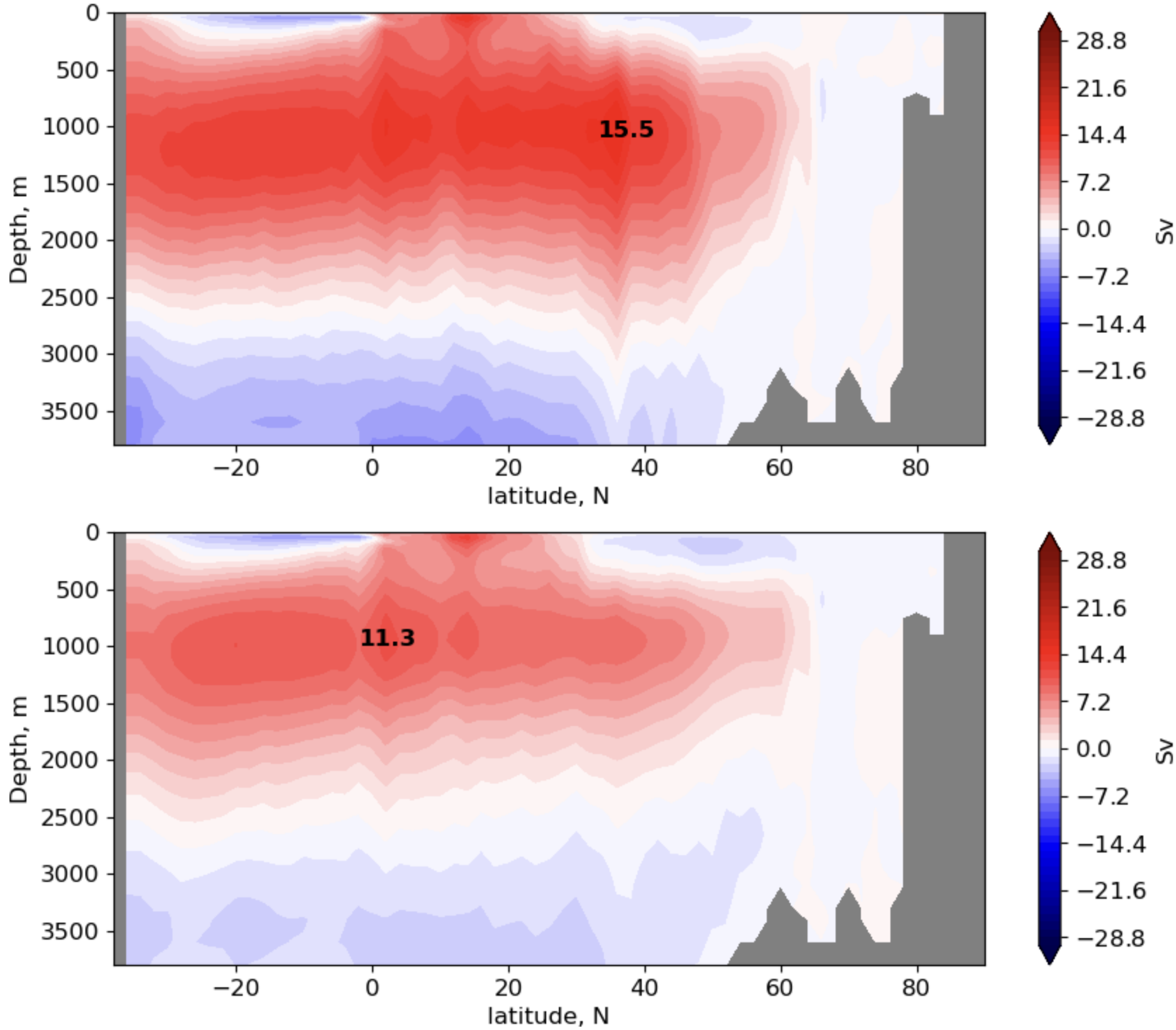

Figure S6: Atlantic Meridional Streamfunction [Sv] for HR simulation, upper: average for years 2000-2009; lower: average for years 2090-2099. The number indicates the maximum value of the streamfunction in the northern Hemisphere.

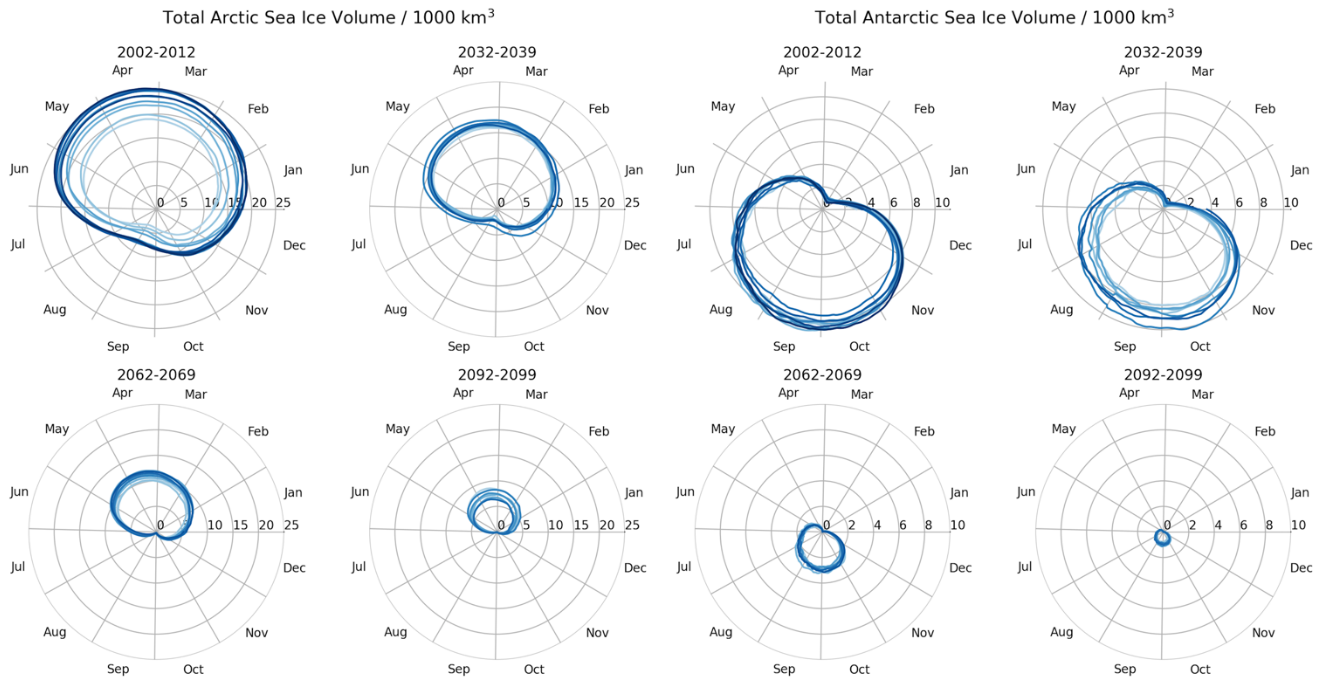

Figure S7: Seasonal cycle of sea-ice volume in Arctic Ocean (left) and Southern Ocean (right) for 2000s and 2030s HR snapshot simulations. Unit [1000 km^3]. The sea ice amplitude in the phase-wheel diagram is represented by the radius and the seasonal phase by the angle.

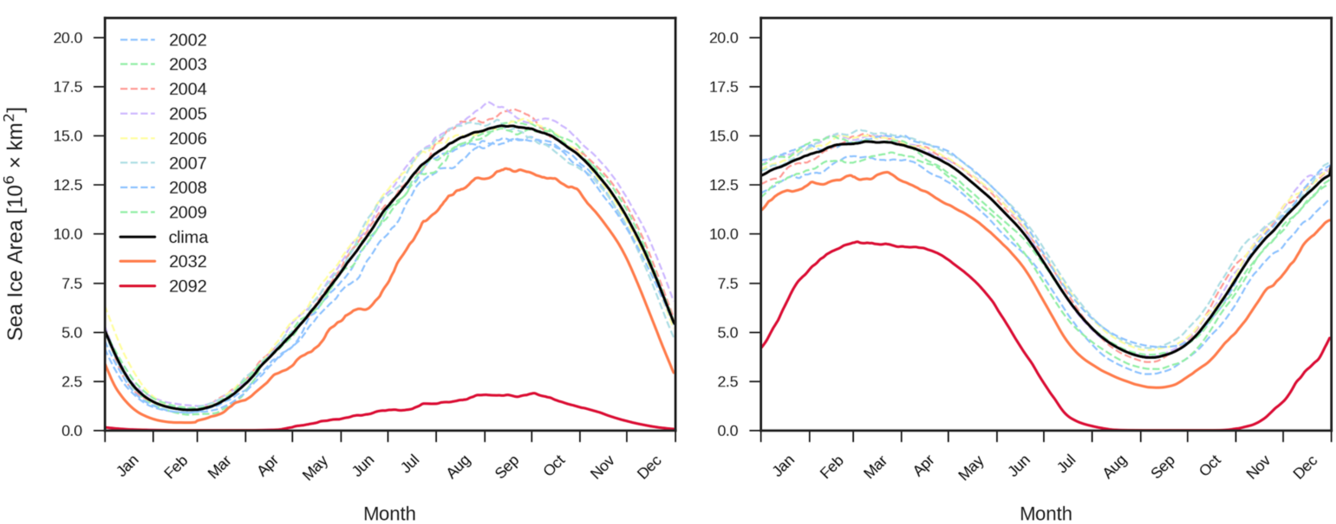

Figure S8: Seasonal evolution of sea ice area in Southern Ocean (left), Arctic Ocean (right) for individual years from 2002-2009, climatology and for future snapshot simulation for years 2032 and 2093.

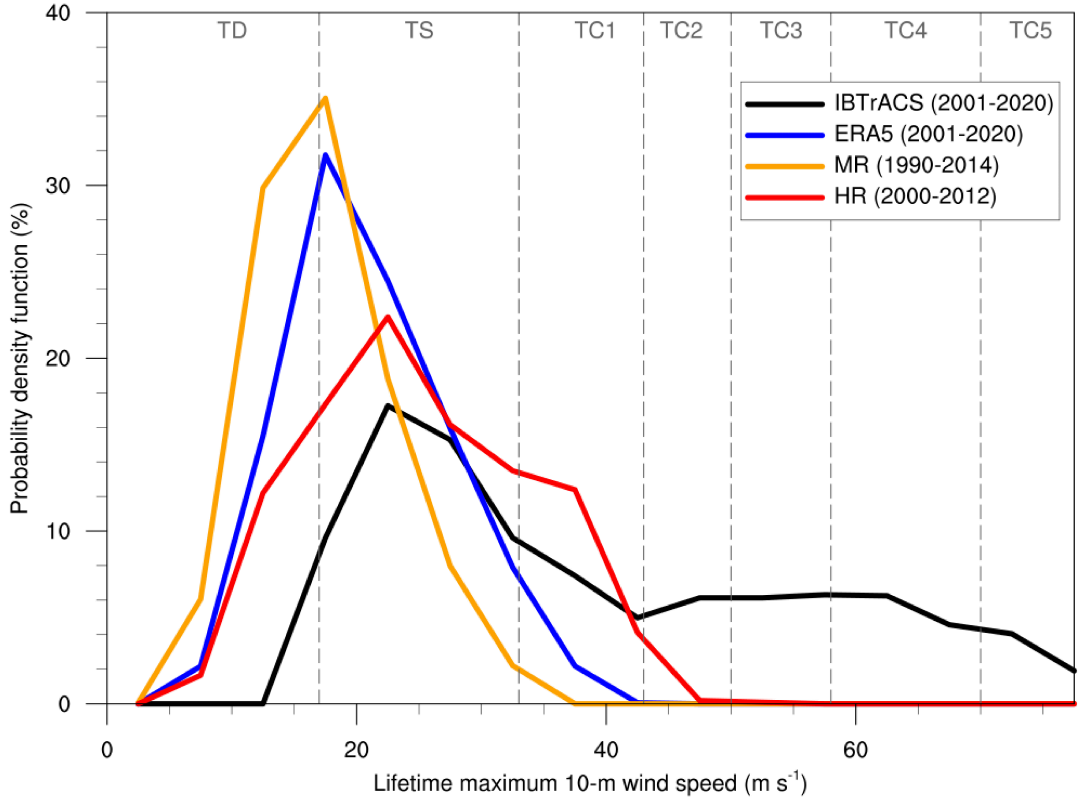

Figure S9: Probability distribution of present-day lifetime maximum 10 m wind speed (ms^{-1}) for tropical cyclones, detected using the OWPZ tracking scheme (see methods in Supplementary S1 and S2) for AWI-CM3 MR and HR simulations. Observation data is obtained from the International Best Track Archive for Climate Stewardship (IBTrACS) best track database version 4 (Knapp et al., 2010).

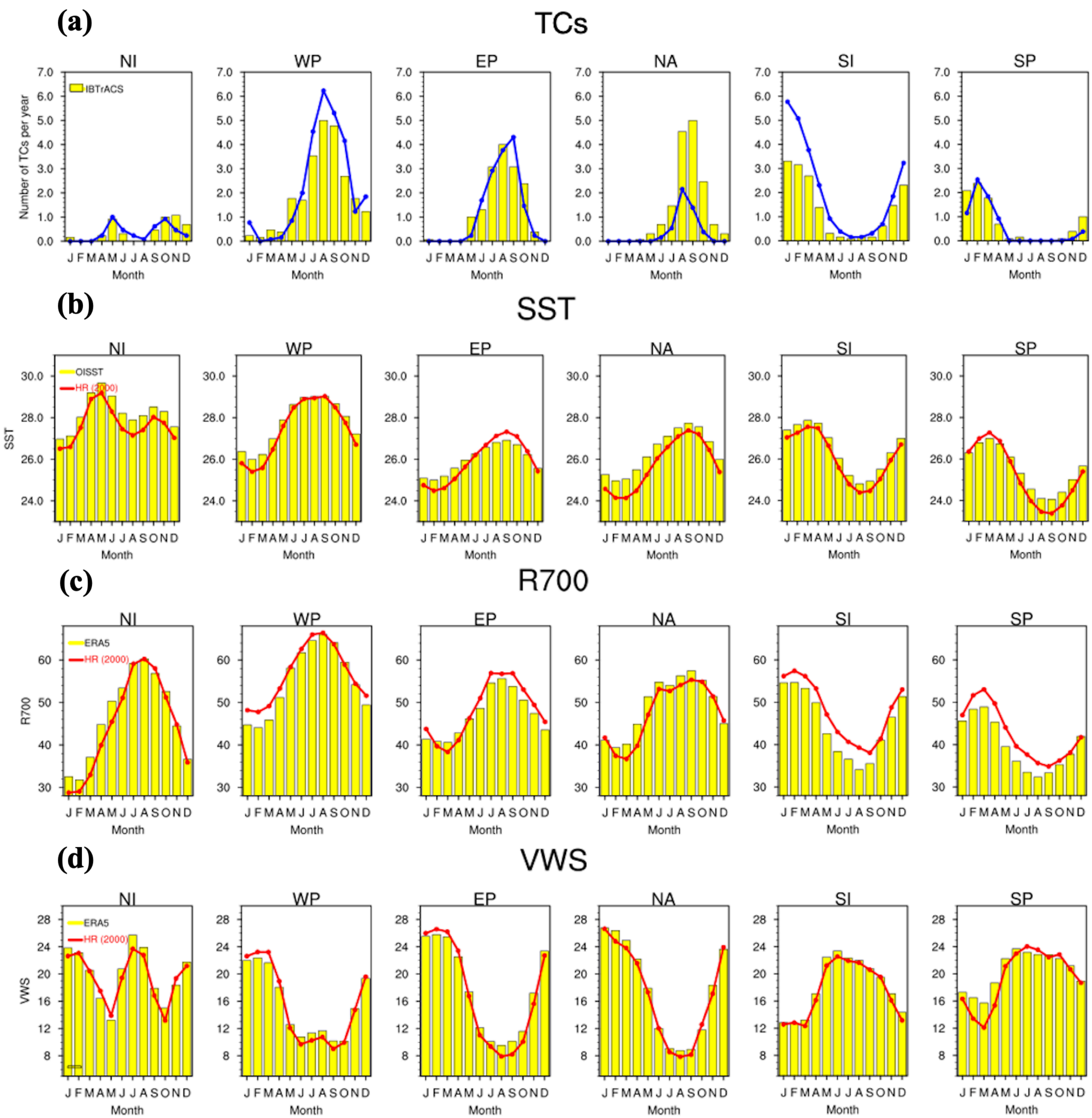

Figure S10: Annual cycle of (a) tropical cyclone genesis frequency, (b) sea surface temperature (SST), (c) relative humidity at 700 hPa (R700), and (d) vertical wind shear between 200 hPa and 850 hPa (VWS) from observation (yellow boxes) and model simulations (thick lines) for each basin. For the comparison of genesis environments, variables in (b)–(d) are averaged within latitude band of 30°S to 30°N. Observation data for SST is obtained from OISSTv2 for SST, while R700 and VWS are derived from the ERA5 reanalysis, averaged over the period from 1991 to 2020.

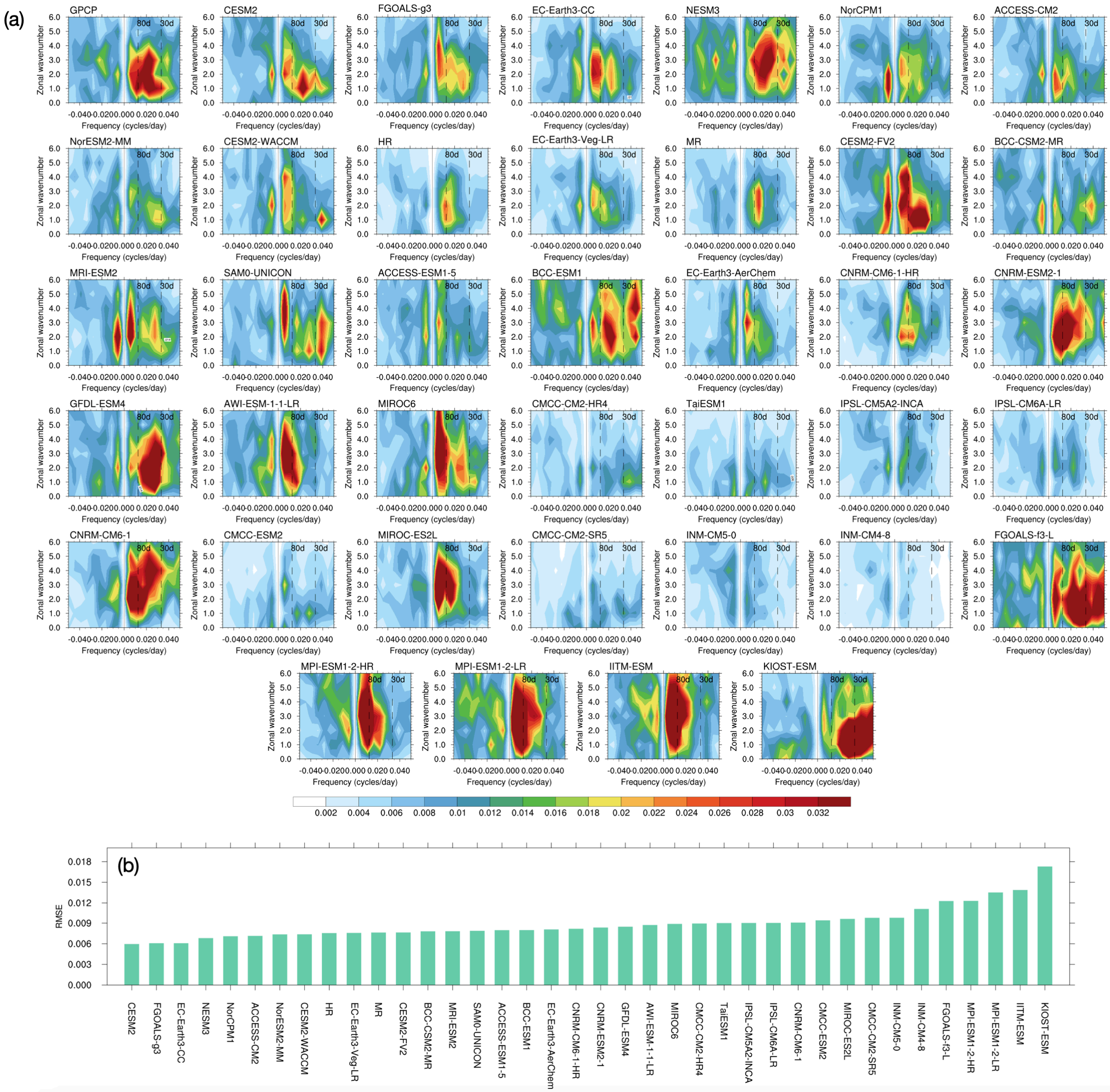

Figure S11: (a) November–April wavenumber-frequency power spectra of 10°S–10°N averaged precipitation from observations (GPCP) and simulations (HR, MR, and 36 CMIP6 models) for the period 2000-2012. (b) Root mean squared error in the spectral domain.

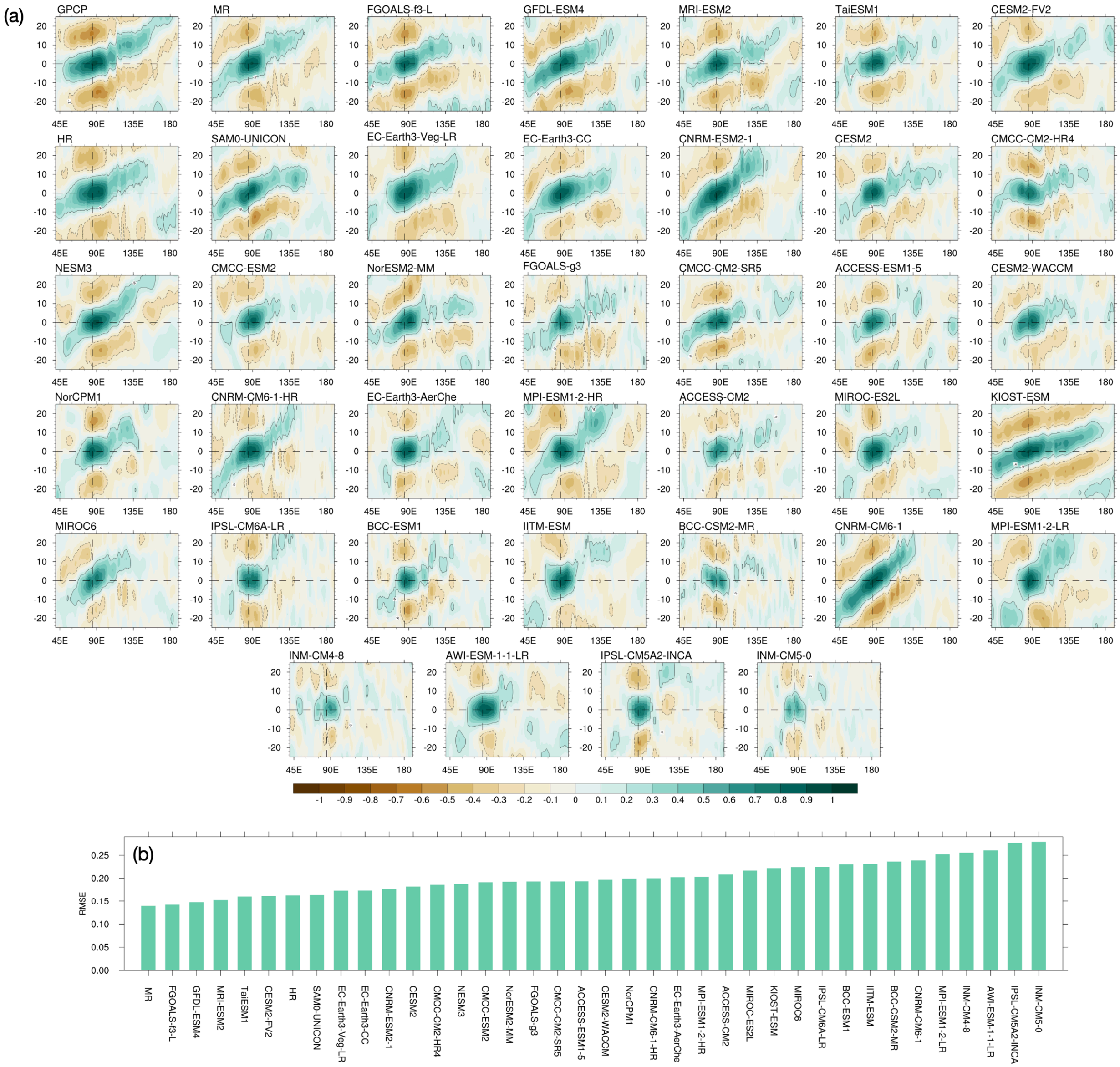

Figure S12: (a) Time lag-longitude correlation of 20-100-day filtered precipitation averaged over 10°S-10°N with reference to the precipitation at the Indian Ocean (10°S-5°N, 75°-100°E) during NDJFMA (period 2000-2012) obtained from observations (GPCP) and simulations (HR, MR, and 36 CMIP6 models). The black contour represents correlation coefficients of ±0.2. (b) Root mean squared error in the time-longitude domain [50°E–180°, from day -20 to day 20].

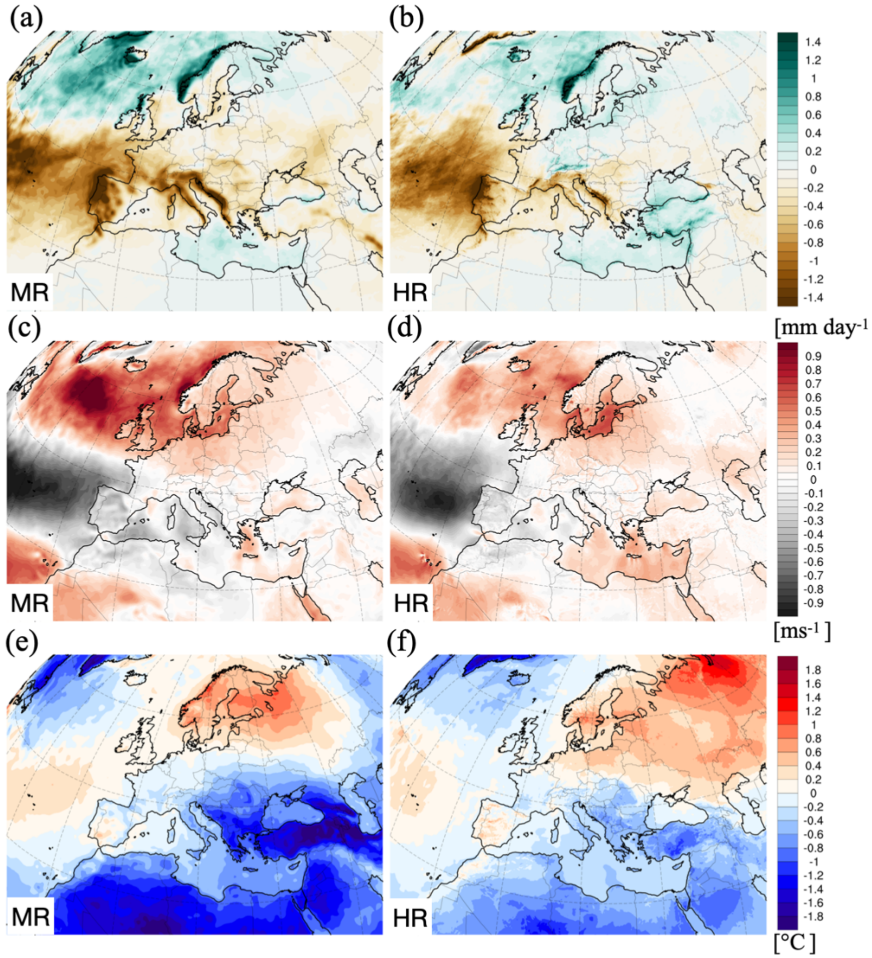

Figure S13: Precipitation (mmday^{-1}) regression with North Atlantic Oscillation Index using 15 years of the MR simulation (2085-2099) (a) and HR simulation (2090-2099 and 2090-2094) (b). (c) and (d), same as (a) and (b), but for the wind speed (ms^{-1}). (e) and (f), same as (a) and (b), but for the surface temperature (°C). The NAO index is based on the leading empirical orthogonal function of DJF seasonal mean sea level pressure anomalies over the North Atlantic and is normalized.

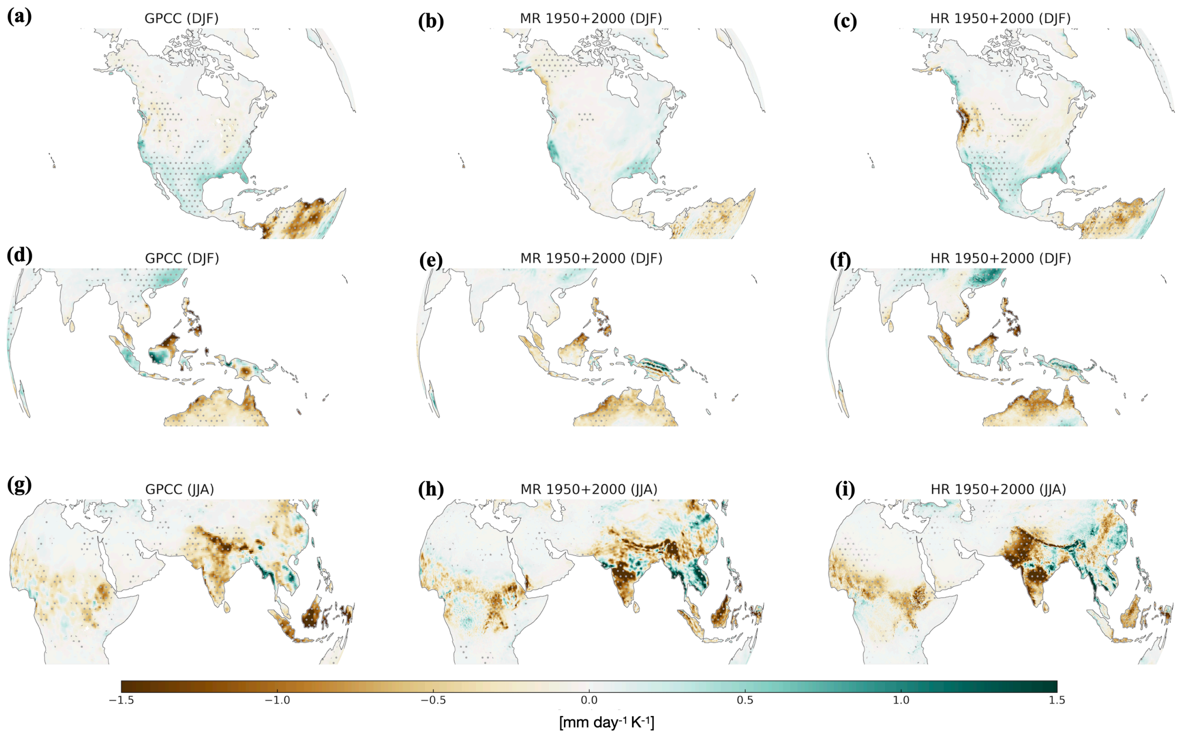

Figure S14: Present-day observed and simulated El Niño teleconnections: Regression between DJF Niño 3.4 SST anomalies with GPCC rainfall observations over North America (a) and Maritime Continent (d) [$\mathrm{mmday^{-1}{}^{o}C^{-1}}$] and JJA Niño 3.4 SST anomalies with GPCC rainfall observations over Indian Ocean (g); (b),(e),(h), same as (a),(d),(g), but for 32 combined years of the MR simulation; (c),(f),(i) same as (a),(d),(g), but for 32 combined years of the 1950 and 2000 HR simulations. The data were detrended prior to the analysis. The stippled areas indicate the regression coefficient values that exceed the 90% confidence level based on the two-tailed Student's t-test (against zero regression). We used the stats module package in Python to perform a two-tailed Student's t-test, assessing whether the regression coefficients significantly differ from zero.

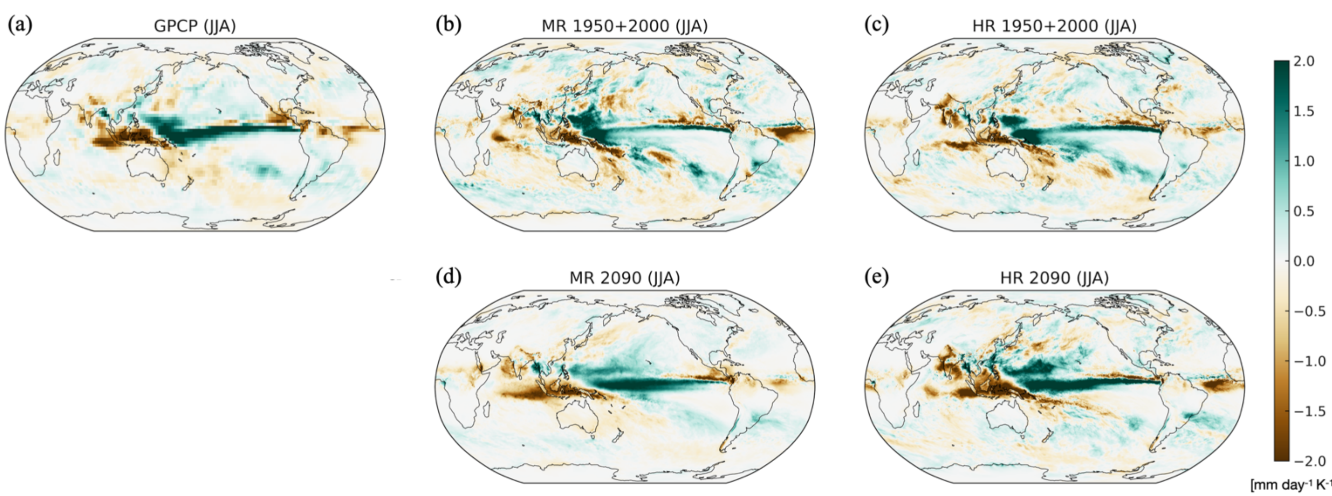

Figure S15: Regression between observed JJA Niño 3.4 SST anomalies and (a) observed rainfall (GPCP); (b) same as (a), but for MR (32 years of present-day climate); (c), same as (a), but for HR (32 years of present-day climate); (d), same (a)(b), but for 2090-2099 period (10+5 years); (e), same as (c), but for 2090-2099 period (10+5 years).

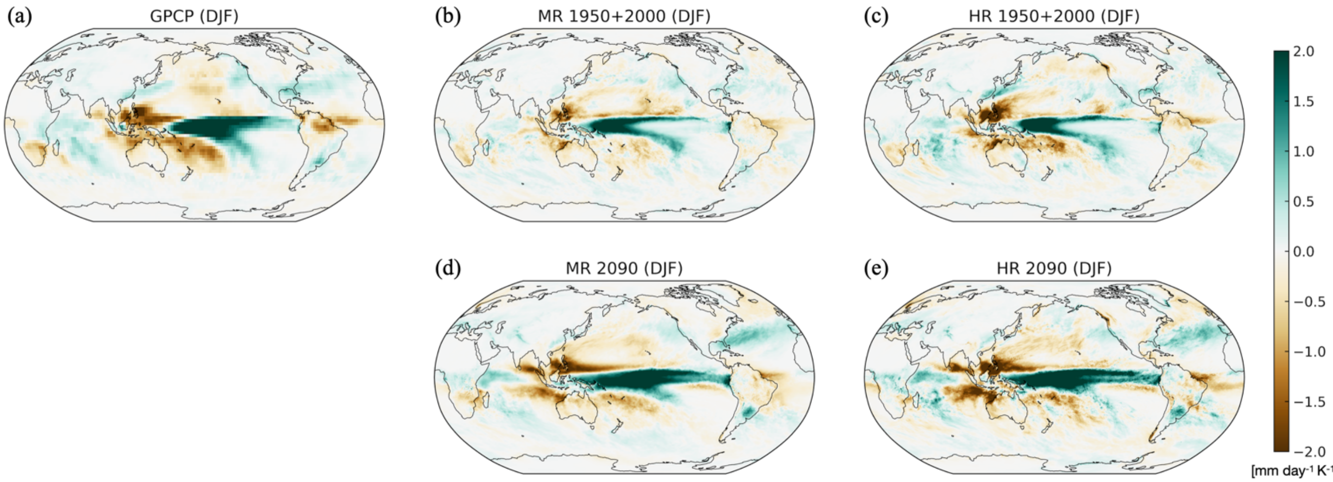

Figure S16: Regression between observed DJF Niño 3.4 SST anomalies and (a) observed rainfall (GPCP); (b) same as (a), but for MR (32 years of present-day climate); (c), same as (a), but for HR (32 years of present-day climate); (d), same (a)(b), but for 2090-2099 period (10+5 years); (e), same as (c), but for 2090-2099 period (10+5 years).

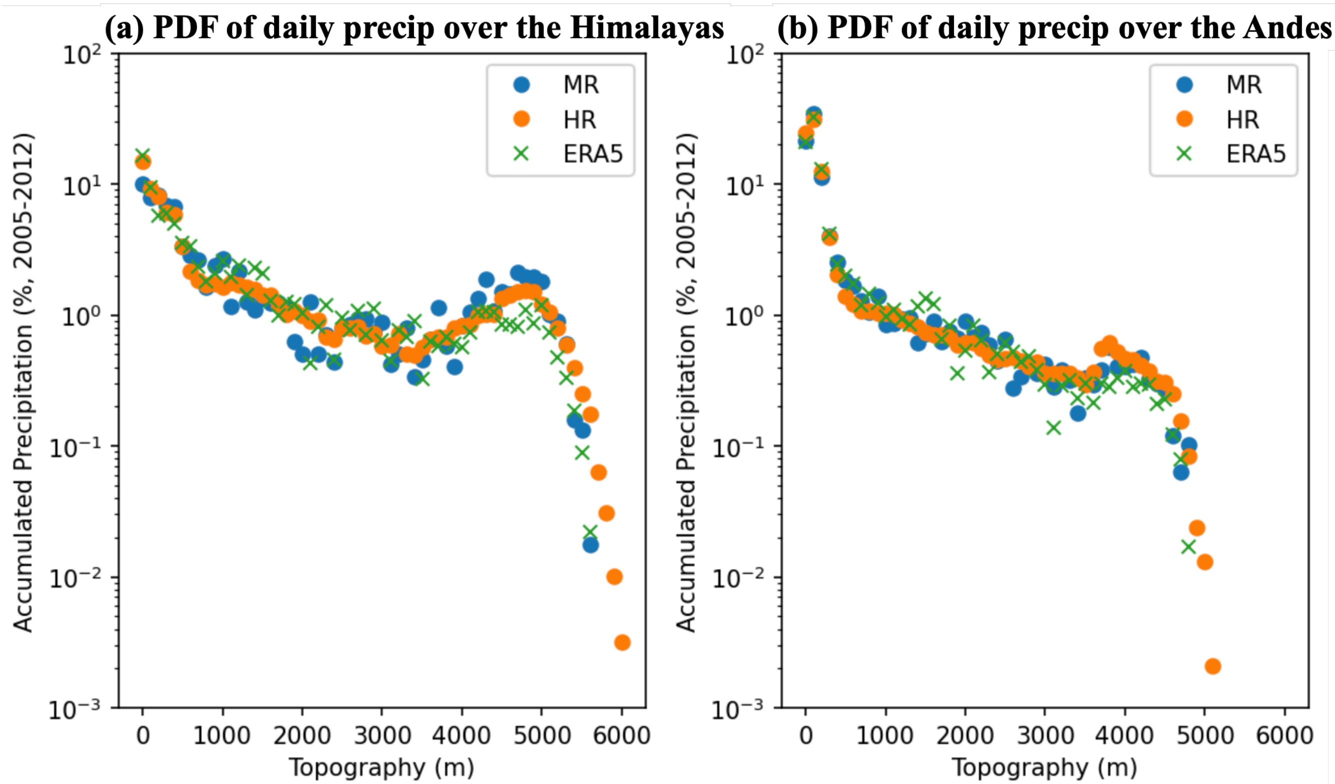

Figure S17: Probability density functions of percentages in accumulated precipitation at each topography bins over (a) the Himalaya region (70°-110°E, 24°-42°N) and (b) the Andes region (northern part, 75°-95°W, 20°S-10°N) for the period 2005-2012 from MR, HR, and ERA5 Reanalysis (25km).

References

Adler, R. F., Sapiano, M. R. P., Huffman, G. J., Wang, J.-J., Gu, G., Bolvin, D., Chiu, L., Schneider, U., Becker, A., Nelkin, E., Xie, P., Ferraro, R., and Shin, D.-B.: The Global Precipitation Cli- matology Project (GPCP) Monthly Analysis (New Version 2.3) and a Review of 2017 Global Precipitation, Atmosphere, 9, https://doi.org/10.3390/atmos9040138, 2018.

Good, S. A., Martin, M. J., and Rayner, N. A.: EN4: quality controlled ocean temperature and salinity profiles and monthly objective analyses with uncertainty estimates, J. Geophys. Res.-Oceans, 118, 6704-6716, https://doi.org:10.1002/2013JC009067, 2013.

Hersbach, H., Bell, B., Berrisford, P., Biavati, G., Horányi, A., Muñoz Sabater, J., Nicolas, J., Peubey, C., Radu, R., Rozum, I., Schepers, D., Simmons, A., Soci, C., Dee, D., and Thépaut, J.-N.: ERA5 monthly averaged data on single levels from 1940 to present. Copernicus Climate Change Service (C3S) Climate Data Store (CDS), https://doi.org/10.24381/cds.f17050d7(Accessed on 01-FEB-2024), 2023.

Kato, S., Rose, F. G., Rutan, D. A., Thorsen, T. J., Loeb, N. G., Doelling, D. R., Huang, X. L., Smith, W. L., Su, W. Y., and Ham, S. H.: Surface Irradiances of Edition 4.0 Clouds and the Earth's Radiant Energy System (CERES) Energy Balanced and Filled (EBAF) Data Product, J. Climate, 31, 4501-4527, https://doi.org/10.1175/jcli-d-17-0523.1, 2018.

Knapp, K. R., Kruk, M. C., Levinson, D. H., Diamond, H. J., and Neumann, C. J.: THE INTERNATIONAL BEST TRACK ARCHIVE FOR CLIMATE STEWARDSHIP (IBTrACS) Unifying Tropical Cyclone Data, B. Am. Meteorol. Soc., 91, 363-376, https://doi.org/10.1175/2009bams2755.1, 2010.

Lavergne, T., Surensen, A. M., Kern, S., Tonboe, R., Notz, D., Aaboe, S., Bell, L., Dybkjaer, G., Eastwood, S., Gabarro, C., Heygster, G., Killie, M. A., Kreiner, M. B., Lavelle, J., Saldo, R., Sandven, S., and Pedersen, L. T.: Version 2 of the EUMETSAT OSI SAF and ESA CCI sea-ice concentration climate data records, Cryosphere, 13, 49-78, https://doi.org/10.5194/tc-13-49-2019, 2019.

Platnick, S., Ackerman, S., King, M., Meyer, K., Men- zel, W., Holz, R., Baum, B., and Yang, P.: MODIS atmosphere L2 cloud product (06_L2), NASA MODIS Adaptive Processing System, Goddard Space Flight Center, https://doi.org/10.5067/MODIS/MOD06_L2.006, 2015.

Raavi, P. H., Chu, J. E., Timmermann, A., Lee, S. S., and Walsh, K. J. E.: Moisture control of tropical cyclones in high-resolution simulations of paleoclimate and future climate, Nat. Commun., 14, 6426, https://doi.org/10.1038/s41467-023-42033-8, 2023.

Reichler, T. and Kim, J.: How Well Do Coupled Models Simulate Today's Climate?, B. Am. Meteorol. Soc., 89, 303–312, https://doi.org/10.1175/BAMS-89-3-303, 2008.

Titchner, H. A. and Rayner, N. A.: The Met Office Hadley Centre sea ice and sea surface temperature data set, version 2: 1. Sea ice concentrations,, J. Geophys. Res.-Atmos., 119, 2864–2889, https://doi.org/10.1002/2013JD020316, 2014.

Tory, K. J., Chand, S. S., Dare, R. A., and McBride, J. L.: The Development and Assessment of a Model-, Grid-, and Basin-Independent Tropical Cyclone Detection Scheme, J. Climate, 26, 5493-5507, https://doi.org/10.1175/jcli-d-12-00510.1, 2013a.

Tory, K. J., Chand, S. S., Dare, R. A., and McBride, J. L.: An Assessment of a Model-, Grid-, and Basin-Independent Tropical Cyclone Detection Scheme in Selected CMIP3 Global Climate Models, J. Climate, 26, 5508-5522, https://doi.org/10.1175/jcli-d-12-00511.1, 2013b.

Wielicki, B. A., Barkstrom, B. R., Harrison, E. F., Lee, R. B., Smith, G. L., and Cooper, J. E.: Clouds and the earth's radiant energy system (CERES): An earth observing system experiment, B. Am. Meteorol. Soc., 77, 853-868, https://doi.org/10.1175/1520-0477(1996)077<0853:catere>2.0.co;2, 1996.